International Journal of Nanoelectronics and Materials

In Press, Accepted Manuscript – Note to user

Characterizations of ZNR/P3HT Inorganic-Organic Hybrid Composite as the Thin Film Solar Cell Active Layer Materials

R. A. Rahman[1,2] , M. A. Zulkefle[1,2], S. H. Herman[1,3*] and R, I. Alip[1,4]

[1]Integrated Sensor Research Group, College of Engineering, Universiti Teknologi MARA, 40450 Shah Alam, Selangor, Malaysia
[2]NANO-ElecTronic Centre, College of Engineering, Universiti Teknologi MARA, 40450 Shah Alam, Selangor, Malaysia
[3]Microwave Research Institute, Universiti Teknologi MARA, 40450 Shah Alam, Selangor, Malaysia
[4]Teraherz Sensing and Research Team, RIKEN Center for Advance Photonics, RIKEN, Sendai, Japan

Received 29 October 2021, Revised 3 June 2022, Accepted 20 June 2022

ABSTRACT

Zinc oxide nanorods (ZNR) and P3HT inorganic-organic hybrid composite layers were fabricated and characterized for the application as the active layers in thin film solar cells. The effect of different numbers of P3HT layers on the optical properties was studied. Optimum P3HT thickness on the ZNR was determined to provide a direct electron movement pathway and reduce the leakage current during the measurement process. ZNR was grown using the chemical bath deposition (CBD) method on a spin coated ZnO seed layer. P3HT was deposited on top of the ZNR layer via the sol-gel spin coating route, with the number of P3HT layers varied. As expected, the number of layers or thickness of the P3HT layer affected the morphology as confirmed by the FESEM images. Besides, the crystallinity and optical properties of the ZNR/P3HT films changed due to the increase in thickness. Since absorption is an important characteristic for a good solar cell, the sample with 5 layers of P3HT (5-L) sample was found to be the most promising sample with the optimized thickness (356.48 nm) for the application in solar cells. 5-L sample exhibit the highest absorbance value compared to other samples.

Keywords: active layers, crystallinity, hybrid, inorganic-organic, morphology

1. INTRODUCTION

The typical operation of a solar cell involves absorbing light and then generating excitons. These excitons tend to dissociate, creating pairs [1-3]. Commonly, the dissociation of exciton into free charge carriers occurs at the donor/acceptor interface. Then, the electric field will then sweep away these charge carriers, which are then will be collected at the respective electrodes, and increase the photocurrent [4,5]. Thus, the performance of a solar cell depends on several factors, namely the mobility of the material's charge carrier, the light absorption by the active layer materials, and energy level alignment built-in electric field occurs at the interface of the donor/acceptor [4-7].

To achieve a high-efficiency thin film solar cells, the researchers focused on materials that are nontoxic and not limited in abundance, thus compatible with the large-scale implementation of PVs [8]. Basically, semiconducting organic macromolecules, inorganic nanoparticles, or both (hybrids) were used during the fabrication of this type of thin-film solar cell. Previously, the fabrication and development of inorganic UV photodetectors using numerous inorganic semiconductors such as SiC, GaN, CdSetc, and ZnO had become noteworthy attention among researchers. Most of these materials were chosen due to their wide band gap [9-12]. Among these materials, ZnO becomes a promising candidate because of its morphology which can be reduced in dimensions. This superiority has a strong impact on its characteristic in optoelectronic devices.

*Corresponding Author: hana1617@uitm.edu.my

ZnO is a wide bandgap (~3.37 eV) II-VI compound semiconductor with good electron mobility of range ~205 $cm^2V^{-1}s^{-1}$, besides having a high exciton binding energy of ~60 meV at room temperature [13-14]. It has unique physical properties, such as a wide range of nanostructures family and non-toxicity. A large diversity of morphologies/nanostructures with varying aspect ratios such as nanowires, nanorods, nanobelts, nanotubes, nanosheets and a few more have been reported in many studies. All of these nanostructures and morphologies could be grown by different solutions and physical-based approaches as example sol-gel, hydrothermal, and electrochemical [15-17]. Many nanostructures can be obtained by the chemical bath deposition (CBD) method, with the assistance of several additives and by varying the growth parameters such as temperature, growth duration, and seed layer [18-20]. In solar cell application, the stability of p-type characteristics in ZnO is still a major challenge and issue, even though ZnO is one of the promising candidates for nanostructured devices and n-type characteristics can be easily obtained.

In this context, compositing ZnO with organic semiconductor materials has been described as a suitable candidate as they have comparable device parameters to their inorganic counterparts and simultaneously can be fabricated by easy, simple, and cost-effective solution processing techniques [21-23]. Numerous stable p-type organic conducting polymers, for example, poly (3-octylthiophene) (P3OT), poly(p-phenylene-vinylene) (PPVs), also poly (3-hexylthiophene) (P3HT) can be established and synthesized in the fabrication of various organic optoelectronic devices [24-26]. Usually, common organic semiconductors thin films are amorphous in nature and have low mobility as compared to inorganic semiconductors [27].

For a composite thin film in solar cell application, the thickness of each layer is crucial to be considered. To be specific, in the case of compositing nanorods in another matrix, short circuits could easily happen if the nanorods layer was not fully covered. Other than that, the thickness of the upper layer was also important to be optimized, to ensure that the electron movement has a direct pathway to the electrode. Since the upper layer acts as the photoactive layer, the optimum thickness is required to trap more light during the measurement process. For this reason, the suitable thickness of the photoactive layer needs to be determined to enhance the performance of the solar cells. Thus, the thickness of P3HT photoactive layer was varied by varying the number of spin coated layers covering the n-type ZNR layer. The effect of the P3HT thickness on the optical properties of ZNR/P3HT inorganic-organic hybrid layers was studied.

2. EXPERIMENTAL

ZNR/P3HT composite bilayer film was fabricated on indium tin oxide (ITO) via sol-gel spin coating and the chemical bath deposition (CBD) method. Prior to the deposition of ZNR and P3HT, ITO was cleaned using a standard cleaning process, to eliminate all the contaminants. Ethanol, C_2H_5OH, and deionized water (DI) were used during the cleaning process and sonicated in an ultrasonicator (Hwashin Technology Powersonic 405) for 10 minutes. For the deposition process, there were three different parts, namely deposition of the ZnO seed layer, growing process of ZNR, and deposition of the P3HT layer.

2.1 Deposition of ZnO Seed Layer

To prepare a 0.4M ZnO solution for the seed layer, the sol-gel route was used. A precursor, zinc acetate anhydrate, $ZnAc_2$ was dissolved in 2-methoxyethanol, $C_3H_8O_2$, and monoethanolamine (MEA), $C_2H_7N_{14}$ which act as the solvent and stabilizer respectively. This mixture was stirred at 300 rpm, and 80 °C heat was applied. After 3 hours, the heat was switched off, and the ZnO solution was kept stirred at room temperature for 24 hours, to obtain a clear and homogenous solution.

When the 0.4M ZnO solution was ready, the deposition process of 5 layers seed layer was conducted by spin-coating technique. A cleaned ITO substrate was placed at the center of the spin coater (Laurell Model WS-650MZ -8NPP/Lite) stage, and 10 drops of ZnO solution were dropped. 4000 rpm spin rotation was set for 60 seconds. After that, the seed layer was dried in a furnace (Protherm Furnace PLF 160/5) for 10 minutes at 150 °C. These deposition and drying steps were repeated until 5 layers of the ZnO seed layer were produced. After the 5th layer, the deposition process of the seed layer was completed followed by an annealing step. The seed layer was annealed at 500 °C for 1 hour.

2.2 Growth Process of ZNR by Chemical Bath Deposition

A 0.1M ZnO was prepared as the chemical solution for the growing process. Zinc nitrate hexahydrate, $Zn(NO_3)_2{\cdot}6H_2O$ and hexamethylenetetramine (HMT), $C_6H_{12}N_4$, which function as precursor and stabilizer were dissolved in DI water (solvent). The mixture was sonicated in an ultrasonicator for 30 minutes at 50 °C. After that, the sonicated solution was kept stirred at room temperature for another 3 hours. Prepared 0.1M ZnO solution was poured into a 100 mL Schott bottle, and the ZnO seeded ITO substrate was placed upside down in the center of the bottle. This Schott bottle was immersed in a pre-heated water bath (Memmert, C1-WNB 7SC) for 1 hour, at 95 °C. After 1 hour, the sample was taken out and rinsed with DI water. The grown ZNR was dried at 150 °C for 10 minutes and annealed at 500 °C for 1 hour.

2.3 Deposition of P3HT Layer

P3HT solution was synthesized by dissolving P3HT powder into a solvent, dichlorobenzene (DCB), $C_6H_4Cl_2$. The mixture of P3HT and DCB was stirred for 15 minutes at 300 rpm. Then, the solution was sonicated in an ultrasonicator for 1 hour. When the solution was ready, the deposition process was conducted by spin coating technique. The ZNR sample was placed at the center of the spin coater's stage. 10 drops of P3HT solution were dropped onto the ZNR layer, with the spin rotation set to 3000 rpm for 60 seconds. The deposited layer was let dry at room temperature for 5 minutes. In this study, the number of P3HT layers was varied to find the optimum thickness that could cover the ZNR layer. The number of layers for the P3HT layer was varied from 1 to 5 layers. The deposition and drying process was repeated until the topmost layer was obtained. At the end of the process, all of the deposited and dried samples were annealed at 160 °C for 10 minutes. The low temperature was applied during the annealing process due to the polymer characteristic of P3HT. The schematic for ZNR/P3HT synthesis process is illustrated in Figure 1. All of the fabricated samples were labeled as below:

Table 1 Classification and sample labelling

Type of sample	Label
ZNR	ZNR
1 layer of P3HT	1-L
2 layers of P3HT	2-L

3 layers of P3HT	3-L
4 layers of P3HT	4-L
5 layers of P3HT	5-L

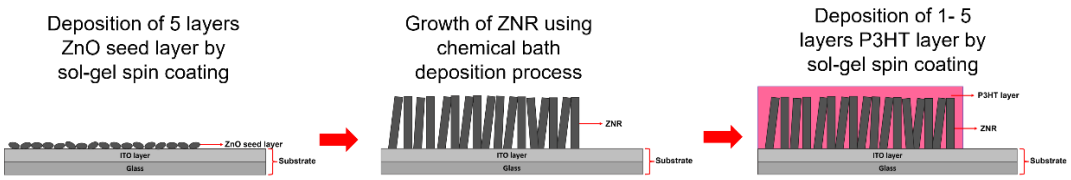

Figure 1. The overall process for deposition of ZNR/P3HT thin film

2.4 ZNR/P3HT Thin Films Characterization

All of the fabricated samples were characterized morphologically, structurally, and optically. A field emission scanning electron microscope (FESEM, JEOL JSM-7600) was used to observe the morphology of the samples. The thickness of the samples was measured by surface profilometer (SP, KLA-Tencor P-6 Stylus Profiler), while for the crystallinity quality, x-ray diffraction (XRD, PANalytical X'PERT PRO) was used. Lastly, all of the samples were characterized by an ultra-violet visible spectrometer (UV-Vis) to determine their optical properties. By using UV-Vis, the transmittance and absorbance of the samples were measured. The optical band gap for all samples was calculated based on the transmittance and absorbance results obtained.

3. RESULTS AND DISCUSSION

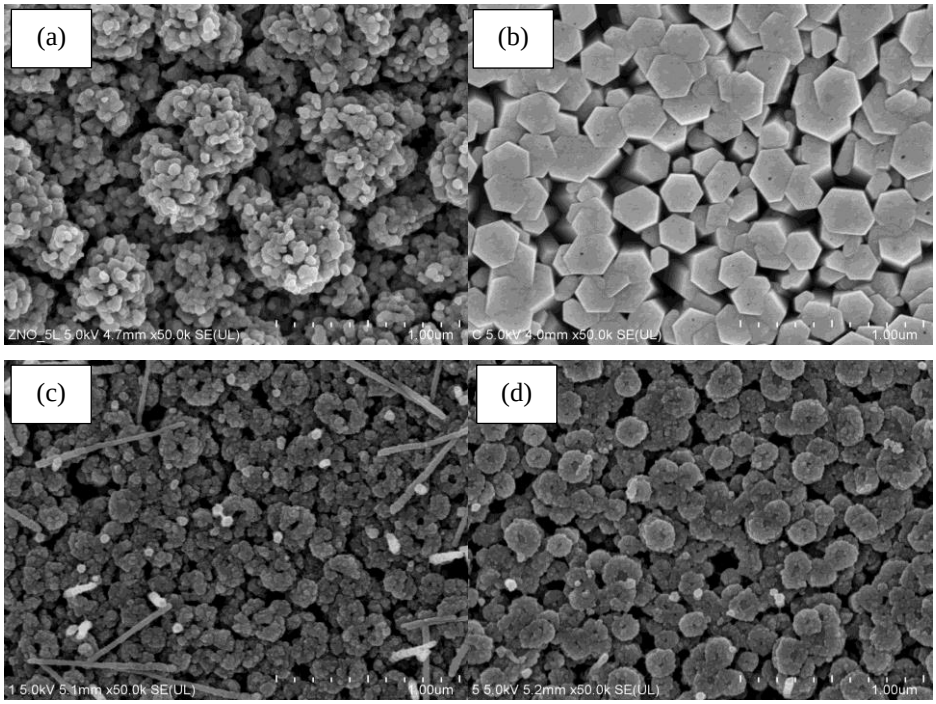

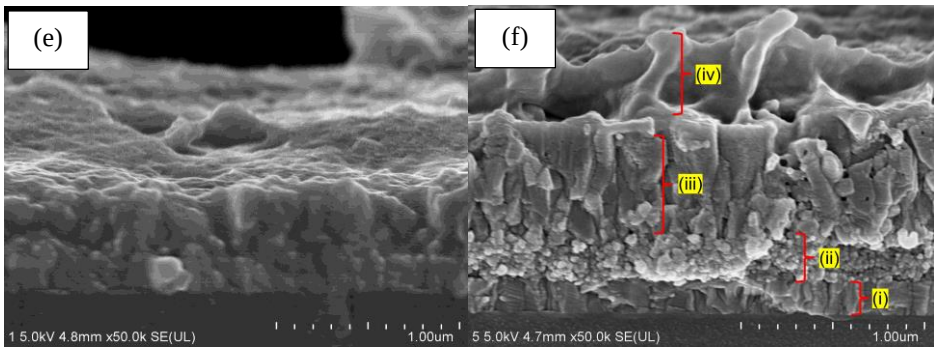

Figure 2. The morphology of (a) ZnO seed layer; (b) grown ZNR; (c) ZNR with 1 layer P3HT; (d) ZNR with 5 layers P3HT; (e) cross section of ZNR with 1 layer P3HT and (f) cross section of ZNR with 5 layers P3HT. (i) – (iv) in (f) indicate the (i) ITO substrate, (ii) ZnO seed layer, (iii) ZNR and (iv) P3HT layer.

Figure 2 shows the morphology of the ZnO seed layer, ZNR, and ZNR/P3HT deposited with 1 and 5-layers of P3HT. From Figure 2 (a), a crack-free, dense, and agglomerated ZnO seed layer could be observed. Deposition of five layers ZnO seed layer produced a uniform distribution of ZnO nanoparticles. It is important to have a uniform and dense seed layer because this seed layer act as the nuclei site for the ZNR. ZNR will be grown according to the morphology of the seed layer prepared. Uniform nuclei sites would assist the growth of ZNR. This can be seen in Figure 2 (b), in which dense and uniform ZNR was successfully grown. Similar phenomena were reported by B. Ikizler et. al. stating that the surface of the parent seeds may serve as nuclei for further growth for the rods [27].

P3HT layers were then deposited on the ZNR. Figure 2 (c) and (d) represent the samples deposited with 1 and 5-Layers of P3HT. The changes in the structures are evident where the size of the particles becomes larger in the 5-layers sample. It can be said that the particles agglomerated when the subsequent layer was deposited. This agglomeration leads to the increasing size of the particles, as shown in Figure 2(d). The increment of the particle's size might be due to the drying process that was conducted after the deposition of each layer. During the drying process, a solid bridge may build up between the particles, thus the agglomeration between the particles occurs [28]. This process continues until all the layers had been deposited. Since the 5-layers was the highest deposition layer, this may be the reason why the particles are bigger compared to the 1-layer ZNR/P3HT film.

Table 2 Classification and sample labelling

Sample	Thickness (nm)
ZNR	321.54
1-L	325.10
2-L	330.14
3-L	337.15
4-L	344.63
5-L	356.48

Other than that, the structure of the 5-layers sample is deduced to have a thicker thickness, proportionally with the number of layers. Generally, the film will have a thicker thickness when the number of layers is deposited. To confirm that the layer of ZNR had been fully covered, a cross-section observation was performed for the 1 and 5-L samples. These cross-sections are labelled as (e) and (f) in Figure 2. However, only 5-L samples show a clear separated layer. Based on the image in Figure 2 (c), four different layers can be observed, (i) the ITO substrate layer, (ii) the ZnO seed layer, (iii) the ZNR layer, and (iv) the P3HT layer. The P3HT layer can be observed to be

on top of the ZNR layer. The SP measurement was conducted to determine the thickness of each of the deposited samples and the results are tabulated in Table 2.

The measured samples exhibit an increasing thickness trend with the increasing number of layers.-As in Table 2, the thickness of the ZNR/P3HT significantly increases, with the 5-L sample having the highest thickness at 356.48 nm, while the sample with 1-layer gave the least thickness value at 325.10 nm. As a reference, the thickness of the ZNR layer was also measured. It can be seen that the deposition of 1 layer of P3HT does not significantly change the total thickness of the sample. This shows that the P3HT acts as the matrix for the nanorods. The second layer of P3HT (as observed in the 2-L sample) was then deposited on the underlying P3HT. It should be noted that as mentioned in the methodology section, a drying process was carried out after the deposition of each P3HT layer. According to a study reported by M. Addamo et al., the drying process during the deposition of each layer might increase the thickness of the film [29]. This means that, when a film is deposited with more than one layer, it will undergo a few times drying processes, thus a thicker film would be produced. This is because during drying each layer grows over irregular and crystalline surface or structure preformed, thereby producing greater thickness. Other than that, the increment of thickness may also be attributed to the increase in the particle quantity of P3HT with the increasing number of layers. During the first layer of P3HT, the P3HT particles had already settled on and between the ZNR layer. When subsequent layers are deposited, the number of particles increases, thereby increasing the thickness of the film. Therefore, the thickness of the thin film increases continuously with the number of P3HT layers.

All samples were also characterized using XRD, to investigate their crystalline quality. Results obtained from this characterization are shown in Figure 3. All samples were deposited with a different number of P3HT layers, and also the bare ZNR sample exhibited a polycrystalline structure based on the XRD results. ZNR sample exhibits three dominant peaks that belong to (100), (002), and (101) planes, while other minor peaks that belong to ITO substrate were identified. On the other hand, for the samples deposited with different P3HT layers, two major peaks for ZNR was observed in all samples which are at the (002) and (101) plane. The peak intensities decrease as the P3HT thickness increases. A peak at 25.77° can be observed for the 5-L sample which is attributed to P3HT(010). The decrease of ZNR peaks with increasing P3HT layer thickness probably can be related to the reduction in ZNR crystalline quality or due to the ratio of P3HT to ZNR layers of which, increasing P3HT peak will relatively reduce the ZNR peaks.

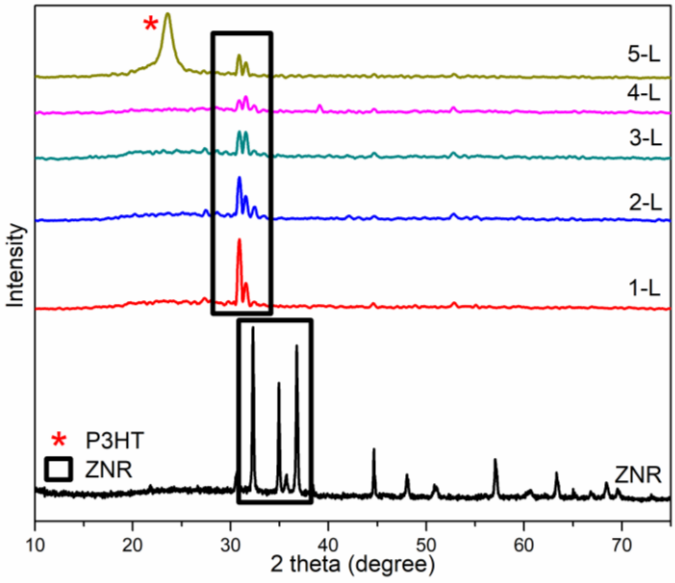

Figure 3. XRD spectra for ZNR, 1-L, 2-L, 3-L, 4-L, and 5-L samples

From the XRD spectra, full width at half maximum (FWHM), the crystallite size (D), dislocation density (δ) and interplanar spacing (d), lattice constant (C_{002}) were calculated by referring to (002) plane. Strain, $\varepsilon_{zz,}$ and stress, σ were also calculated and tabulated in Table 2. D was calculated using Scherer's formula, according to the eq. (1) below:

$$D = \frac{0.94\lambda}{\beta \cos\theta} \quad (1)$$

Referring to the eq. (1), D is the crystallite size for the samples, obtained according to the crystallographic peaks in XRD spectra, λ is the x-ray wavelength (1.542 Å), β is the diffraction line broadening at half of the maximum intensity (FWHM) of the peak, and θ is the Bragg's angle of diffraction in radian (obtained from 2θ). From the determination of D, dislocation line density was calculated, using eq. (2) and interplanar spacing, d for all peaks were determined using eq. (3)

$$\delta = \frac{1}{D^2} \quad (2)$$

$$d = \frac{n\lambda}{2\sin\theta} \quad (3)$$

According to the eq. (2), dislocation line density was obtained by dividing 1 by the value of crystallite size, calculated using eq. (1). D in eq. (2) referring to the value of calculated crystallize size. For interplanar spacing, d, n=1 is the order value of diffraction, while λ is the same value used in eq. (1), which is the x-ray wavelength (1.542 Å), and θ is the Bragg's angle of diffraction, which is the same value used for D calculation.

While for the lattice constant, c, the values were obtained by referring to the eq. (4), below:

$$c = \frac{\lambda}{\sin\theta} \quad (4)$$

Here, λ is the constant value of wavelength for the x-ray radiation source (0.154 Å) and θ is the value obtained from 2θ in the spectra. As for the strain, $\varepsilon_{zz,}$ and stress, σ, the values were calculated based on the eq. (5) and (6) below:

$$\varepsilon_{zz} = \frac{c_{film} - c_{bulk}}{c_{bulk}} \, x \, 100\% \quad (5)$$

$$\sigma = \frac{2c_{13}^2 - c_{33}(c_{11c} + c_{12})}{2c_{13}} \quad (6)$$

For eq. (5), C_{film} signifies the lattice parameter of the ZnO nanorod films and C_{bulk} is the unstrained lattice parameter for bulk ZnO (5.2066 Å). According to the equation used to calculate the stress, C_{ij} is the elastic stiffness constant of bulk ZnO (C11=208.8 GPa, C12=119.7 GPa, C13=104.2 GPa, and C33=213.8 GPa) and ε_{zz} is the lattice strain obtained from eq. (5). The film thickness may influence the thin film crystalline quality including the formation of strain and stress in the lattice [30]. The positive and negative strain values represent the tensile strain when the film is stretched and the compressive strain when the film is compressed [31]. In short, if the value is positive, it is considered a tensile strain, otherwise, it is considered a compressive strain. While for stress, if the value obtained is positive, it is considered tensile stress, and the negative value indicates the compressive stress [31]. As seen in Table 3, the diffraction angle (2θ) for (002) peak

in samples composited with the P3HT layer had shifted to a smaller angle when a further number of layers were deposited. As observed from the XRD spectra, the ZNR sample has a higher angle of (002) peak, compared to samples with P3HT layers. By referring to the X. Zhao et al., the diffraction angle might shift when a thin film/material was composited with another material [32]. This shifting may due to the lattice mismatch between the transition layer and the thin film and also the stress between two layers in the composited bilayer thin film [32].

Table 3 Crystallinity properties (FWHM, crystallite size, dislocation line density, lattice constant, strain and stress) for ZNR deposited with different number of layers of P3HT

Samples	2θ (°)	FWHM	Crystallite size, D (nm)	Dislocation line density, δ (δ x 10^{-3} line/nm^2)	Interplanar spacing, d (Åm)	Lattice constant (c_{002})	Strain, εzz (%)	Stress, σ, (GPa)
ZNR	35.06	0.4019	36.77	0.740	2.5594	5.112	-1.8150	4.22
1-L	34.60	0.4262	34.67	0.832	2.5927	5.179	-0.5300	1.23
2-L	34.58	0.4462	32.94	0.922	2.5941	5.18	-0.4724	1.09
3-L	34.57	0.4485	32.75	0.932	2.5949	5.183	-0.4533	1.05
4-L	35.55	0.4515	31.97	0.978	2.5963	5.186	-0.3957	0.92
5-L	34.52	0.5082	29.07	1.183	2.5985	5.190	-0.3188	0.74

Other than that, composite bilayer film is different from the film that was composited during the solution preparation and doped film. Composited bilayer film does not involve the combination and composition of two different materials in the same solution. A doped or composite film usually will shift the diffraction angle to a higher value, different from the composite bilayer film, which shifts the diffraction angle to a lower value, as obtained in this study. The main reason behind this occurrence is, that composite bilayer film does not affect the atom arrangement or substitution process in both materials [33]. Besides, the crystallite size, lattice constant, strain, and stress for all P3HT samples also have the same trend with the diffraction angle, which is a decrement trend. These outcomes may be ascribed to the variations in the crystallographic properties of the films. All of these properties decrease, as the thickness/number of P3HT layers increases. In this study, the negative value of strain emerges for compressive strain, while the stress value is positive, which indicates tensile stress for all samples. Y. Q. Dai et. al, stated that the variation in these properties occurs due to the thickness of the film that increases significantly, thus causing stress relaxation [34].

Optical properties for all of the deposited samples were characterized using UV-Vis. Transmittance and absorbance spectra for ZNR and ZNR/P3HT deposited with the different

number of P3HT layers were measured in the range of 350-800 nm. Figure 4 shows transmittance, while Figure 5 presents the absorbance spectra for all the samples, respectively.

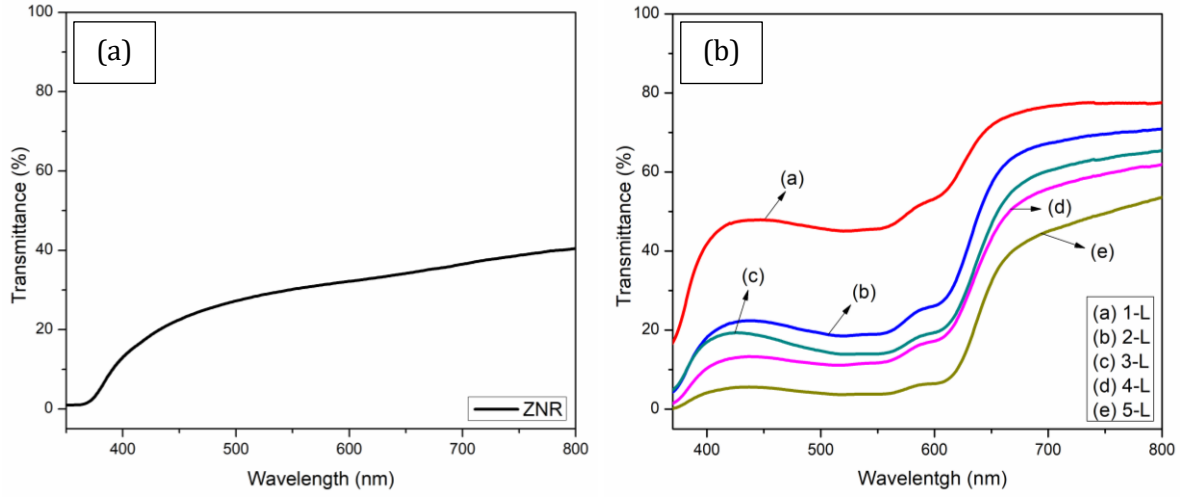

Figure 4. Transmittance spectra for (a) ZNR and (b) ZNR/P3HT samples

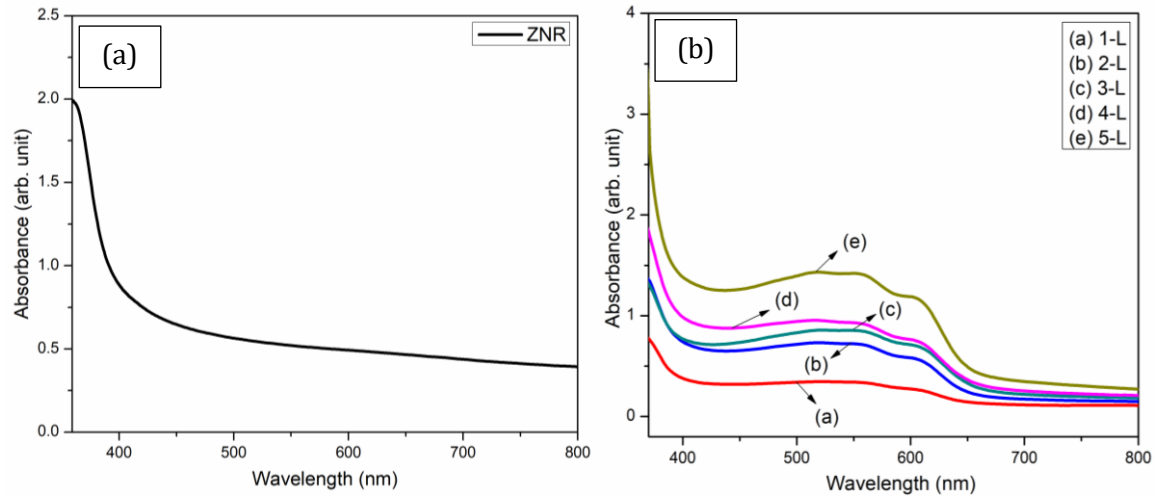

Figure 5. Transmittance spectra for (a) ZNR and (b) ZNR/P3HT samples

Figure 4 exhibits the transmittance for all deposited samples. The value of the transmittance rapidly drops and apparently decreases as the number of P3HT layers increases. In this study, it could be clearly observed that the transmittance spectra for the samples changed when been composited with P3HT. As shown in Figure 4 (a), ZNR transmittance spectra have a transmission peak at ~400 nm, while for samples composited with P3HT, two vibrionic shoulders at ~550 nm and ~605 nm existed. The vibrionic shoulders are clearly visible when the number of P3HT layers was increased. Generally, the absorbance value will have an inverse relationship with the transmittance value. As can be observed in Figure 5 the 1-L sample has the least absorbance value and the 5-L sample shows the highest absorbance value. The thickness of the film is the major reason for this. When a film has a thicker thickness, the light that enters through the film has a longer traveled path, thus the film could trap more light, resulting in a low value of transmittance and a higher value of absorbance. Results obtained in this measurement proved that the thickness plays an important role, in determining the optical properties of the ZNR/P3HT films. For further investigation, the optical energy band gap was estimated, using Tauc's plot. Figure 6 shows the estimation graph for all samples deposited in this study.

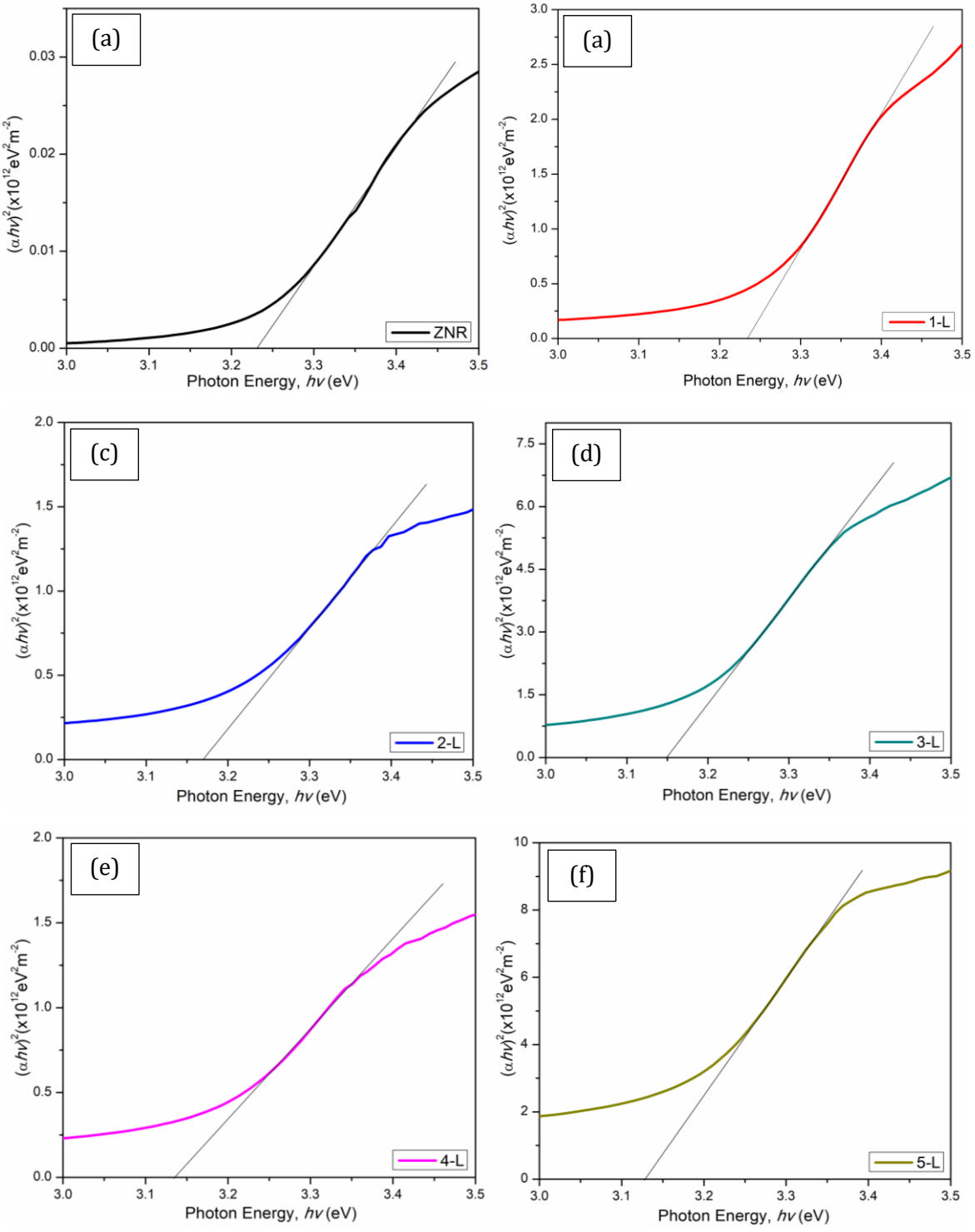

Figure 6. Tauc's plot for E_g estimation of ZNR and ZNR deposited with different numbers of P3HT layers

The change in the optical energy band gap, E_g reflected the effect of the number of P3HT layers on the optical properties of ZNR/P3HT films. The E_g value was obtained from Tauc's relation, as expressed in equation (7).

$$(ahv) = B\ (hv - E_g)^n \quad (7)$$

The estimated values of E_g are provided in Table 4.

Table 4 Crystallinity properties (FWHM, crystallite size, dislocation line density, lattice constant, strain, and stress) for ZNR deposited with different numbers of P3HT layers

Samples	Optical Band Gap Value (eV)
ZNR	3.23
1-L	3.21
2-L	3.17
3-L	3.13
4-L	3.13
5-L	3.12

In this study, it was found that the E_g values are in the range of 3.1 ~ 3.2 eV, the highest is from the bare ZNR sample which is 3.23 eV. The optical band gap value started to decrease when the P3HT layer was deposited and decreased continuously as the number of P3HT layers increased. When the number of P3HT layers is increased, the thickness of the P3HT layers affected the optical band gap of the samples because of the low P3HT band gap (~1.9 eV), due to which indirectly, leads to the decrement of the overall E_g value for all of the samples. On the other hand, thickness increment may introduce some of the defects in film, which will create the localized state in the band-gap, thus affecting the value of the E_g [35]. Similar results were also observed in the studies reported by S. Sonmezoglu et. al, and H/ B. Yao et. al [36,37].

4. CONCLUSION

ZNR/P3HT thin films were successfully fabricated via sol-gel spin coating and chemical bath deposition methods. From this study, the influence of the P3HT layer on the optical characteristics of the samples was investigated, where the number of P3HT was varied from 1 to 5 layers. In the comparison, the bare ZNR layer (without the P3HT layer on top) was also characterized. FESEM images revealed that the presence of the P3HT layer changed the morphology of the ZNR, the thickness of the samples increased when the number of P3HT layers was increased. From the FESEM and surface profiler characterization, the 5-L sample exhibit the highest thickness, with a value of 356.48 nm. It was evident from the FESEM image that the ZNR layer was fully covered when deposited with 5 layers of the P3HT layer on top. Compositing ZNR and P3HT had also affect the crystallinity of the samples, in which the (002) peak was seen shifted to the lower angle when more P3HT layers were deposited on the ZNR. These changes also influenced the other crystallinity properties, such as FWHM, D, d, lattice constant, stress, and strain. As the thickness of the samples increased, the optical properties were also affected. The transmittance value shows a decrement trend, while the absorbance value increased as the thickness of the films increased with the addition of P3HT layers. This occurrence had led to the changes in optical band gap value. The optical band gap decreased from 3.23 eV for the sample without the P3HT, to 3.21 with 1 layer of P3HT and further reduced to the lowest, 3.12 for the sample with 5 layers of P3HT. Based on the characterization process conducted, fabricated ZNR/P3HT thin films have the potential to be applied in solar cell applications. From the analysis, the 5-L sample is the most suitable sample to be applied as solar cells, due to the highest absorption value, and has the suitable thickness to fully cover the ZNR layer. It is important to cover all of the ZNR layers to avoid and reduce the short circuit during the solar cell measurement process.

ACKNOWLEDGEMENTS
The authors would like to thank all members of Nano Electronic Center (NET), Integrated Sensors Research Group (DERIA), and Nano-Science Technology Center (NST, Universiti Teknologi MARA (UiTM) Shah Alam for all the research facilities. This work is partially supported by Geran Inisiatif Penyeliaan (GIP)(Project code: 600-IRMI/GIP 5/3(024/2021))

REFERENCES

[1] Wang, X., Song, W., Liu, B., Chen, G., Zhou, C., Shen, G., Advanced Functional Material. vol. **23**, issue 2013 (2013) pp.1202-1209.
[2] Li, H-G., Wu, G., Shi, M.-M., Yang, L.-G., Chen, H-Z., Wang, M., Applied Physics Letters. vol. **93**, issue 2008 (2008) pp.153309.
[3] Wang, J.-J., Wang, Y.-Q., Cao, F.-F., Guo, Y-.G, Wan, L.-J., Journal of the American Chemical Society. vol. **132**, issue (2010) pp. 12218–12221.
[4] Bilgaiyan, A., Dixit, T., Palani, I. A., Singh, V., Journal of Electronic Materials. vol. **44**(2015) pp.2842–2848.
[5] Dou, L., Yang, Y., You, J., Hong, Z., Chang, W.-H., Li, G., Yang, Y., Nat Commun. vol. **5**, issue 5404 (2014) pp.1-6.
[6] Manekkathodi, A., Lu, M.-Y., Wang, C. W., Chen, L.-J., Adv Mater. vol. **22**, issue 36 (2010) pp.4059–4063.
[7] K. Lee, H. Park, C. H, K. Lee, T. Ha, J. H. Kim, J. Yun, G-H. Lee, S. Im., Organic Electronics. vol. **12** issue 7 (2011) pp.1103–1107.
[8] Luceño-Sánchez, J., Díez-Pascual, A., Peña Capilla, R., Int. J. Mol. Sci. vol. **20**, issue 4 (2019) pp.976.
[9] Lee, D. J., Ryu, S. R., Kumar, G. M., Cho, H. D., Kim, D. Y., Ilanchezhiyan, P., Applied Surface Science. vol. **558**, (2021) pp. 149896.
[10] Yildirim, M. A., Teker, K., , Journal of Alloys and Compounds. vol. **868** (2021) pp.159255.
[11] Huo, Z., Zhang, Y., Han, X., Wu, W., Yang, W., Wang, X., Zhou, M., Pan, C., Nano Energy. vol. **86**(2021) pp.106090.
[12] Li, X., Tong, X., Yue, S., Liu, C., Channa, A. I., You, Y., Wang, R., Long, Z., Zhang, Z., Zhou, Z., Liu, X-F.,. Wang, Z. M., Nano Energy. vol. **89**, issue A (2021) pp.106392.
[13] Özdal, T., Kılıç, M., Kavak, H., Superlattices and Microstructures. vol. **156** (2021), pp.106948.
[14] Boumezoued, A., Guergouri, K., Regis, B., Rechem, D., Zaabat, M., Materials Today: Proceedings. (2021) pp. 1-5.
[15] Ortega, P. P., Silva, C. C., Ramirez, M. A., Biasotto, G., Foschini, C. R., Simões, A. Z., Applied Surface Science. vol. **542,** (2021) pp.148723.
[16] Faisal, M., Harraz, F. A, Jalalah, M., Alsaiari, M. A., Al-Sayari, S. A., Al-Assiri, M. S., Materials Today Communications. vol. **24** (2020) pp.101048.
[17] Baran Aydın, E., Sığırcık, G., International Journal of Hydrogen Energy. vol. **44**, issue 23 (2019) pp. 11488-11502.
[18] Suma, M. N., Prasad, M. V. N., Gaddam, V., Rajanna, K., Nayak, M. M., Materials Today: Proceedings. vol. **24**, issue Part 3 (2020) pp.1713–1719.
[19] Mahajan, S., Jagtap, S., Effect of reaction temperature and time on the physical properties of CTAB-assisted hydrothermally grown ZnO nanostructures. Materials Today: Proceedings, (2021) pp.1-6.
[20] Chongsri, K., Boonyarattanakalin, K., Pecharapa, W., Materials Today: Proceedings. vol. **5**, issue 6 (2018), pp.14110–14115.
[21] Verma, R., Pathak, S., Srivastava, A. K., Prawer, S., Tomljenovic-Hanic, S., Journal of Alloys and Compounds. vol. **876** (2021) pp.160175.
[22] Chan, Y. Y., Pang, Y. L., Lim, S., Chong, W. C., Journal of Environmental Chemical Engineering. vol. **9**, issue 4 (2021) pp.105417.
[23] Lv, Y., Liu, J., Zhang, Z., Zhang, W., Wang, A., Tian, F., Zhou, W., Yan, J., Materials Chemistry and Physics. vol. **267** (2021) pp.124703.
[24] Yadav, A., Upadhyaya, A., Gupta, S. K., Verma, A. S., Negi, C. M. S., Thin Solid Films. vol. **675** (2019) pp.128-135.

[25] Benchaabane, A., Belhadi, J., Ben hamed, Z., Lejeune, M., Lahmar, A., Sanhoury, M. A., Kuoki, F., Zellana, K., Zeinert, A., Bouchriha, H., Materials Science in Semiconductor Processing. vol. **41** (2016) pp.343–349.
[26] Al-Asbahi, B. A., Qaid, S. M. H., Ghaithan, H. M., Farooq, W. A., Journal of Non-Crystalline Solids. vol. **552** (2021) pp.120429.
[27] Ikizler, B., and Peker, S. M., Thin Solid Film. vol. **558** (2014) pp.149–159.
[28] Magsoodi, M., Yari, Z., Iran. J Pharm Res. vol. 14, issue 1 (2016) pp.51-57.
[29] Addamo, M., Augigliaro, V., Di Paola, A., Garcia-Lopez, E., Loddo, V., Marci, G., and Palmisano, L., Thin Solid Films. vol. **516**, issue 12 (2008) pp.3802-3807.
[30] Abadias, G., Chason, E., Keckes, J., Sebastiani, M., Thompson, G. B., Barthel, E., Doll, G. L., Conal, E., Stoessel, C. H., Martinu, L., Journal of Vacuum Science & Technology A: Vacuum, Surfaces, and Films. vol. **36**, issue 2 (2018) pp.020801.
[31] Zhang, Q., Huang, G., Li, S., Crystals. vol. **10**, issue 6 (2020) pp.488.
[32] Zhou, Y.-E., Tan, X.-Y., Yu, B.-F., Liu, L., Yuan, S.-L., Jiao, W.-H., Chinese Physics Letters. vol. **31**, issue 3 (2014) pp.037304.
[33] Hasan, M. R., Lai, C. W., Bee Abd Hamid, S., Jeffrey Basirun, W., International Journal of Photoenergy. vol. **2014**, 2014 (2014) pp.141368.
[34] Dai, Y. Q., Dai, J. M., Tang, X. W., Zhang, K. J., Zhu, X. B., Yang, J., Sun, Y. P., Journal of Alloys and Compounds. vol. **587**(2014) pp.681–687.
[35] Ben Rabeh, M., Khedmi, N., Fodha, M. A., Kanzari, M., Energy Procedia. vol. **44** (2015) pp.52-60.
[36] Sönmezoğlu, S., Arslan, A., Serin, T., Serin, N., Physica Scripta. vol. **84**, issue 6 (2011) pp.065602.
[37] H. B. Yao, L. P. Shi, T. C. Chong, H. Meng, P. K. Tan, X. S. Miao, International Symposium on Optical Memory and Optical Data Storage Topical Meeting. **2002** (2002) pp.99-101.

International Journal of Nanoelectronics and Materials

In Press, Accepted Manuscript – Note to user